C.A. Wang

A New Organometallic Vapor Phase Epitaxy Reactor for Highly Uniform Epitaxy

We have designed and built a new organometallic vapor phase epitaxy (OMVPE) reactor for the growth of thin films of compound semiconductors such as GaAs and AlGaAs. The reactor grows highly uniform and reproducible epitaxial layers that can be fabricated into various electronic and optoelectronic devices. To obtain such precision, we designed the reactor by using both gas-flow visualization and numerical modeling. The design results in uniform laminar flow and short gas residence times, which are critical for obtaining uniform growth and abrupt interfaces between epitaxial layers over large surface areas. High-performance quantum-wall diode lasers designed to pump solid state lasers have been fabricated from such uniform layers.

The development of thin-film deposition processes for compound semiconductors is crucial to the advancement of sophisticated electronic and optoelectronic devices. High-speed electronic transistors, quantum-well diode lasers, light-emitting diodes, photodetectors, and optical modulators are fabricated from structures composed of numerous epitaxial layers (epilayers) that range in thickness from several micrometers to as thin as a few tenths of a nanometer. These epilayers are deposited, or grown, on a single-crystal substrate whereby under the proper conditions the epilayer replicates the substrate so well that the two are often indistinguishable.

One technique for forming epilayers is molecular-beam epitaxy (MBE). In MBE, beams of atomic or molecular species impinge upon a heated substrate placed in an ultrahigh-vacuum environment. The process results in the growth of an epitaxial film on the substrate surface. Although MBE has enabled the demonstration of various new devices [1], the slow deposition rates of the process have limited its widespread use.

Another thin-film technique is organometallic vapor phase epitaxy (OMVPE), which is also referred to as metal-organic chemical vapor deposition (MOCVD). In OMVPE, gaseous organometallic (OM) and hydride precursors are transported by a carrier gas to a hot substrate. Near the substrate surface, the gases pyrolyze and deposition occurs by the recombination of atomic or molecular species. The thickness and composition of the epilayers that are formed can be controlled by adjusting various parameters such as the concentration of precursors, carrier-gas flow rate, reactor pressure, and growth time.

Since OMVPE's first demonstration 20 years ago [2], researchers have made considerable progress in perfecting the growth technology—for example, by improving the purity of the precursor materials. OMVPE has gained rapid acceptance in the semiconductor industry over the past five years because of the process's capability and versatility in producing a wide range of extremely pure compounds and alloys at growth rates several times that of MBE. Using OMVPE, researchers have fabricated virtually every advanced semiconductor device. The process, however, has had one serious drawback: precise control of a film's thickness, composition, and doping over large areas has heretofore been unattainable. Such control is critical because advanced circuit concepts require the fabrication of multilayer structures that are highly uniform over large substrate areas.

This article describes the development of an OMVPE reactor capable of producing high-quality epilayers of III-V compound semiconductors, i.e., semiconductors that consist of elements from Groups III and V of the periodic table. The epilayers have extremely uniform

thicknesses, alloy compositions, and doping with nearly atomically abrupt interfaces between successive layers. We begin with a description of the basic OMVPE process, and then discuss the gas-dynamics study that was essential for the design and operation of the new reactor. This study, which involved flow visualization and numerical modeling, was performed in collaboration with the Department of Chemical Engineering at MIT. We then present uniformity results for test wafers and for diode lasers fabricated from structures grown in the reactor. The results are the best reported to date.

Fundamentals of OMVPE

In OMVPE, an epitaxial thin film is deposited on a heated single-crystal substrate by the pyrolysis of gaseous OMs and hydrides. For example, the deposition of GaAs and the ternary alloy $Al_xGa_{1-x}As$ proceeds via the following reactions:

$$Ga(CH_3)_3 + AsH_3 \xrightarrow{\Delta} GaAs + 3CH_4\uparrow,$$

and

$$xAl(CH_3)_3 + (1-x)Ga(CH_3)_3 + AsH_3 \xrightarrow{\Delta} Al_xGa_{1-x}As + 3CH_4\uparrow.$$

In this process, the film constituents are transported in a flowing gas, typically H_2, through an open-tube reactor to the substrate. The film constituents are in the form of a metal-alkyl vapor, i.e., trimethylgallium (TMG) and trimethylaluminum (TMA); and a hydride, i.e., arsine. Epitaxial deposition occurs by the pyrolysis of the source gases and subsequent recombination of the atomic or molecular species at or near the substrate. The partial pressures of the metal-alkyl vapors determine the composition of the ternary alloy. Typical growth temperatures range from 600° to 800°C.

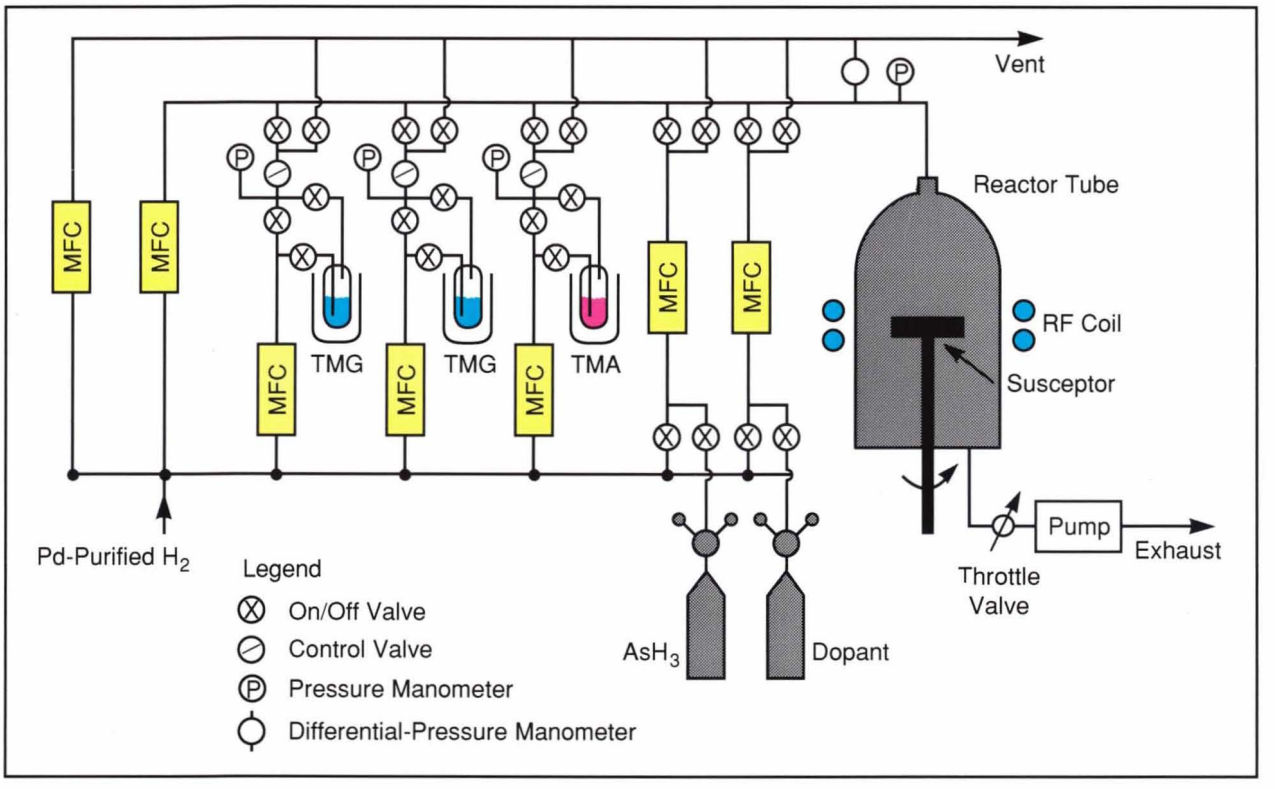

Fig. 1—Schematic diagram of OMVPE gas system. Mass flow controllers (MFC) regulate the flow rates of the gas mixtures to the reactor tube. H_2 is the carrier gas used. Stainless steel bubblers contain the trimethylgallium (TMG) and trimethylaluminum (TMA).

In general, the overall reaction is

$$MR_n + XH_n \xrightarrow{\Delta} MX + nRH \uparrow,$$

in which R is an organic radical such as CH_3^* or $C_2H_5^*$, M is the metallic constituent of the film, X is the nonmetallic constituent, and n is an integer that is dependent on the valences of M and X. Note that if metal alkyls and hydrides of different elements are mixed, a variety of Group III-V, II-VI, and IV-VI ternary and quaternary semiconducting compounds can be obtained in a manner similar to that used in the fabrication of GaAs and AlGaAs. (Because the hydrides are highly toxic gases, some laboratories have replaced them with OM sources that are much less hazardous [3]).

Figure 1 is a schematic of a typical gas system. An automated gas manifold delivers the gas mixtures to the reactor and the flow rates are controlled by electronic mass flow controllers (MFC). Highly purified H_2 is most often the carrier gas used. The OMs are typically highly volatile liquids or solids that are contained in stainless steel bubblers; the hydrides are gases at room temperature and are contained in high-pressure cylinders.

The volume flow rate of an OM source entering the reactor (f_{OM}) is given by $f_{H_2}(P_{OM}/P_{total})$, in which f_{H_2} is the flow rate of H_2, the carrier gas; P_{OM} is the partial pressure of the OM source; and P_{total} is the total pressure in the bubbler. Temperature-controlled baths that surround the OM bubblers keep P_{OM} for each source constant. If pressure-control systems are used to maintain fixed total pressures, then the OM supplies to the reactor can be controlled by precise metering of the H_2 carrier gas.

The OMVPE system at Lincoln Laboratory consists of six pressure-controlled liquid source lines and four hydride lines. Each reactant and dopant gas line is connected to a common fast-switching gas manifold from Thomas Swan, Ltd. For sharp compositional interfaces between successive epilayers, the gas mixtures in the reactor must be exchanged rapidly; i.e., the residence times of the reactants need to be kept as small as possible. Therefore, the manifold design minimizes unswept volumes (dead spaces) that serve as virtual gas sources and increase the residence time.

In the growth of heterostructures, carrier gas flows through the source bubblers during the entire growth-process period. The reactant gas normally flows to a bypass (or vent) line, and is then switched into the reactor (or run) line at the appropriate time. This mode of operation is commonly referred to as vent-run [4]. To prevent pressure surges during switching sequences [5], the system restricts the differential pressure between the vent and run lines to less than 1 Torr.

The entire gas manifold is constructed of stainless steel parts: welded lines and pneumatically operated high-vacuum valves with sealed bellows. Metal-to-metal seals are the preferred method of connecting the parts. A computer that controls the MFCs and valve sequencing improves the system's ability to grow and reproduce epilayers having specified properties.

The most widely used types of reactors are horizontal, vertical, and barrel (Fig. 2). The horizontal and barrel reactors are similar in that the gas flow is nearly parallel to the substrate. In vertical reactors, the flow is perpendicular. All three types of reactors consist of a quartz tube and a heated susceptor on which substrates are placed. Susceptors are made of either graphite or SiC-coated graphite and are heated by either inductive or radiative means.

Typically, horizontal and vertical reactors produce a single wafer in a growth run. In contrast, the multifaceted susceptor used in barrel reactors can hold as many as 20 5-cm-diameter wafers.

During epilayer growth, process gases that are introduced at one end of the reactor convect and diffuse through the reactor to the substrate surface. The gases then flow to the exhaust line at the opposite end. The reactor operates at atmospheric pressure, or at a reduced pressure obtained by means of a vacuum pump. Finally, scrubbers in the exhaust line remove toxic substances from the effluent.

To a large extent, a reactor's configuration and system pressure govern the gas flow and the transport of heat and mass, fluxes that all greatly influence the deposition process. Under

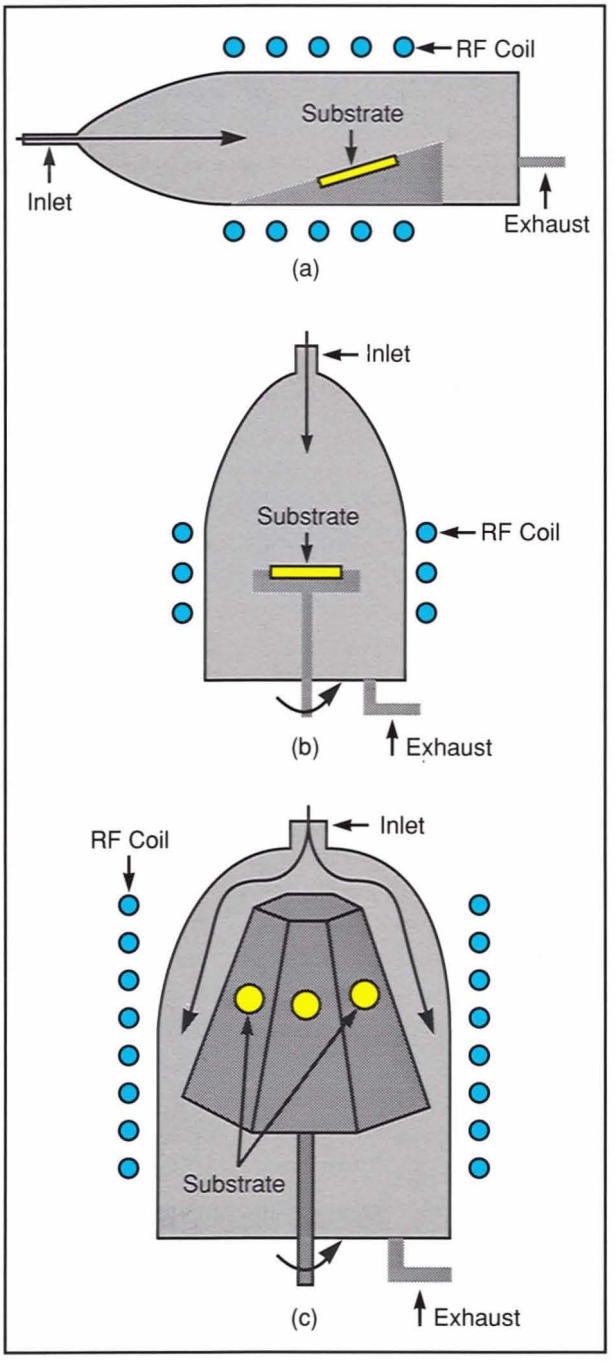

Fig. 2—Three types of reactors used in OMVPE: (a) horizontal, (b) vertical, and (c) barrel.

typical conditions, epitaxial growth is mass-transport-limited; i.e., deposition occurs by the diffusion of the reactants through a boundary layer (Fig. 3). Within the boundary layer, the reactant concentration changes from an initial composition to a reduced value near the growth interface. Epilayer uniformity and interface

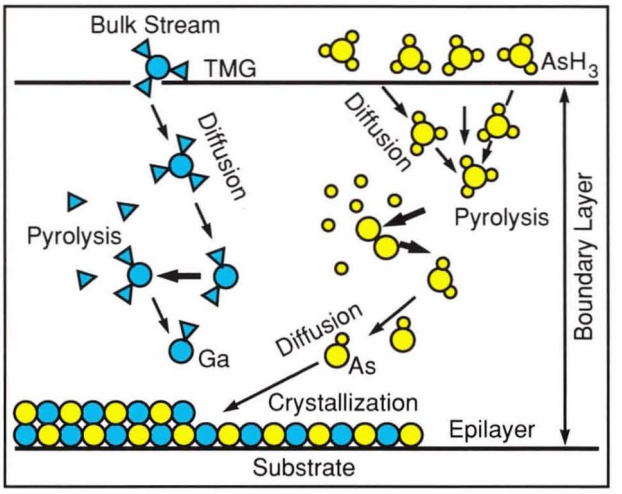

Fig. 3—Representation of boundary layer at the substrate surface. The transport of reactants through the boundary layer occurs by diffusion. The characteristics of the boundary layer are determined by the gas velocities, temperature and concentration gradients, chemical species, and reactions that occur near the boundary layer.

abruptness depend only on the composition of the reactants adjacent to the substrate and thus on the transport of these species through the boundary layer. The characteristics of the boundary layer are determined by the gas velocities, temperature and concentration gradients, chemical species, and reactions that occur near the boundary layer. Several general points are worth noting:

- The boundary layer controls the epilayer growth rate and composition.
- Uniform growth and homogeneous epilayer properties require a constant gas flux over the entire substrate surface.
- For abrupt compositional interfaces between epilayers, the flow field in the reactor should be free of vortices, which trap source gases and increase gas residence times.

Reactor Development

The gas dynamics in a reactor greatly influence epilayer quality; uniformity and abrupt compositional changes between layers require precise control of the gas flow adjacent to the substrate as well as throughout the reactor. In designing the reactor, we used a light-scattering technique developed at Lincoln Laboratory to

visualize the gas flow in the reactor [6]. This technique, which is similar in principle to one used in wind tunnels for investigating wind shear effects on aircraft [7], employs a sheet of laser light as the light source. The laser restricts observation to vertical cross-sectional planes, thus permitting detailed observation of the gas-flow patterns. Numerical methods were used to construct a theoretical model of the reactor fluid flow and heat and mass transfer [8]. A detailed numerical analysis simulated the epitaxial growth in the reactor and established the critical parameters for fabricating uniform epilayers having abrupt compositional changes between the layers. We performed the visualization and simulations with full-scale systems that incorporated 5-cm-diameter wafers—the standard size that the industry uses for laser fabrication.

Gas-Flow Visualization

Figure 4 is a schematic of the apparatus that was used for the gas-flow visualization. The vertical quartz tube, which has an inner diameter of 10 cm, contains a rotating RF-heated susceptor disk made of graphite. The distance between the disk, which is 6.7 cm in diameter, and the gas inlet is 15 cm. A vacuum pump and control valve in the exhaust section of the system permit low-pressure operation. We studied two methods of introducing gas into the quartz tube: (1) a vertical pipe inlet coaxial with the tube, and (2) a radial inlet above a 7.6-cm-diameter porous plug formed by metal screens.

Gas-flow patterns are revealed by the scattering of laser light from TiO_2 particles that are generated by the reaction of $TiCl_4$ and H_2O and transported through the tube by a carrier gas. We use helium, whose properties are similar to H_2, as the carrier gas to simplify the apparatus. Vertical cross sections through the tube are illuminated with a sheet of light formed by directing the beam of a 5-mW He-Ne laser through a cylindrical lens. Since the intensity of scattered light is proportional to the local concentration of TiO_2 particles, gas mixing in the tube can be observed by tracing the paths of these particles following their introduction into the tube. We can estimate gas residence times by measuring the time required for particles to clear the tube after the generation of smoke is stopped by bypassing the $TiCl_4$ bubbler.

In OMVPE reactors, the most common method of gas injection is through a pipe inlet that is coaxial with the reactor tube. For such a setup, Figs. 5(a), 5(b), and 5(c) are cross-sectional photographs showing gas-flow patterns that were obtained at room temperature with a total flow rate of 2 standard liters per minute (slpm) and a tube pressure of 1 atm. A jet extending from the inlet to the susceptor disk (Fig. 5[a]) is observed 1 s after the initial introduction of smoke. The jet flows radially outward across the disk and strikes the side of the tube. By 20 s (Fig. 5[b]), vortices extending from the top of the disk are observed around the jet. At 20 s the concentration of smoke is higher in the jet than in the vortices, but the concentration in the vortices increases with time because some of the smoke being added becomes trapped there. After smoke generation is stopped, the smoke clears rapidly from the jet and across the disk (Fig. 5[c]), but persists in the

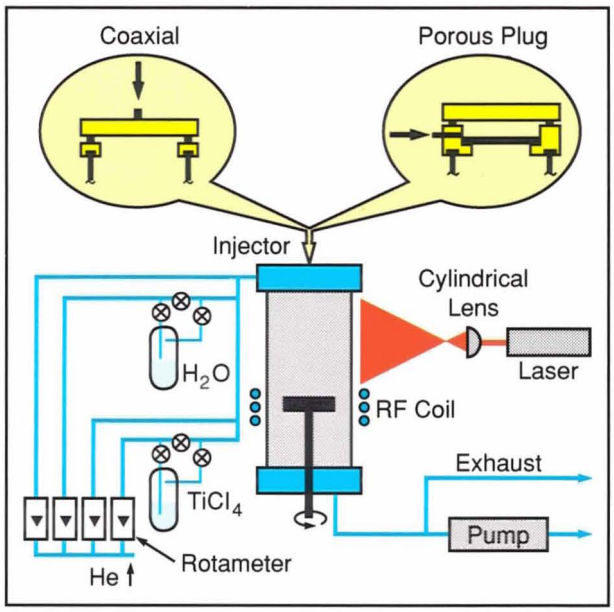

Fig. 4—Schematic diagram of apparatus used for gas-flow visualization. Gas is introduced into the reactor by either a vertical pipe inlet coaxial with the tube or a radial inlet above a 7.6-cm-diameter porous plug formed by metal screens. A 5-mW He-Ne laser illuminates a vertical cross section of the reactor tube to reveal the gas-flow patterns.

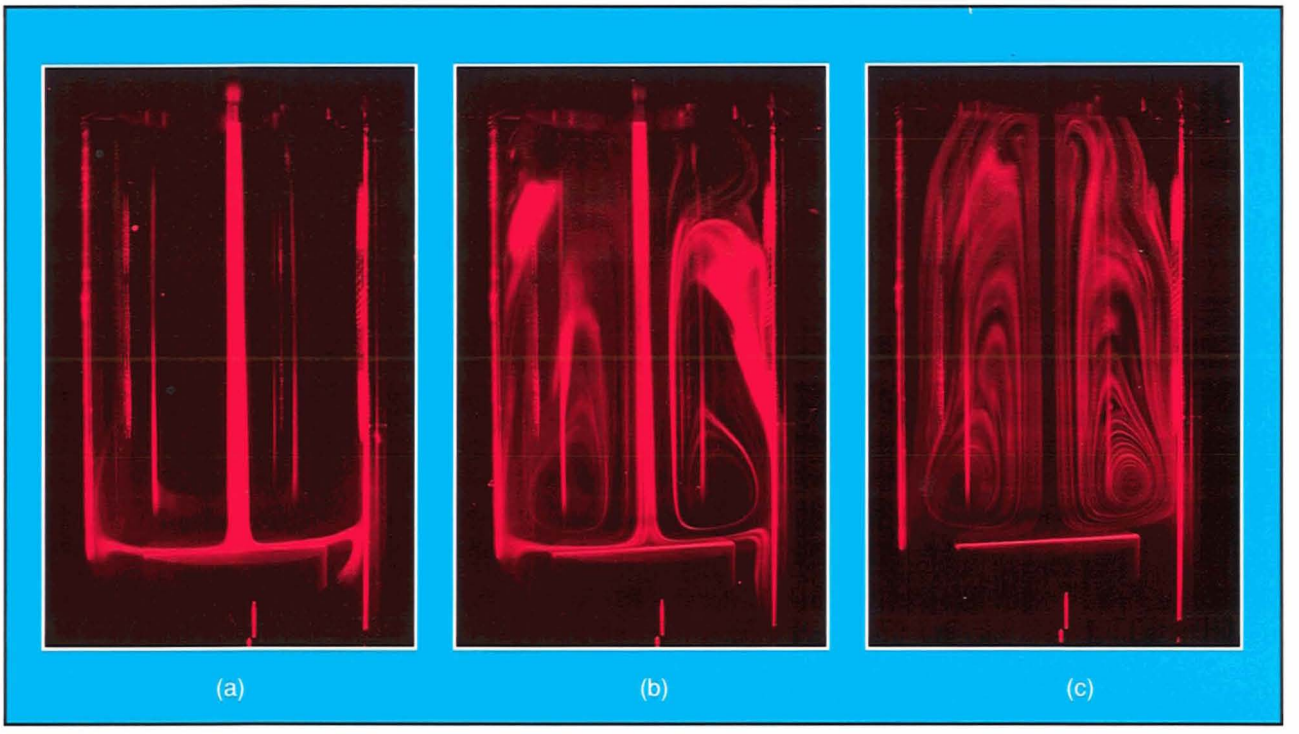

Fig. 5—Vertical cross sections showing flow patterns at room temperature and 1 atm obtained for gas injection through a coaxial pipe inlet: (a) 1 s after initial introduction of smoke; (b) 20 s after initial introduction of smoke; (c) 1 min after smoke was turned off. Intense gas recirculation occurs throughout the reactor as a result of the impinging jet.

vortices for several minutes.

The velocity profile of the gas flow from the pipe inlet is not at steady state when the jet first reaches the disk. As a result of the impinging jet, intense gas recirculation occurs throughout the reactor. An increase in the gas-flow rate increases both the velocity of the jet and the gas-recirculation velocities. Gas trapped in vortices is isolated from the main flow, and its composition changes only by diffusion across the separating streamline. This diffusive control leads to long gas residence times for dopant and alloying components. Consequently, we expect that coaxial injection will result in the growth of epilayers having a high degree of radial nonuniformity and marked grading between layers.

In contrast, the use of a radial inlet followed by a porous plug results in uniform injection over a large cross section of the tube. Figure 6 shows the steady-state flow pattern that was obtained at room temperature, a pressure of 1 atm, and a flow rate of 10 slpm. In our apparatus, gases are injected into an antechamber through an inlet that is radial with respect to the reactor-tube axis. The antechamber is designed to produce turbulent flow for complete mixing of the gases. From the antechamber, the gas flows into the reactor tube through an opening of the same diameter as that of the plug, and the velocity profile of the gas is independent of radial distance—typical characteristics of plug flow. The uniform intensity of smoke particles in the photograph indicates that the gas is mixed well. (Note: the vertical streaks in the photograph are reflections of the laser light from the walls of the tube). The time that elapses before laminar flow reaches the disk is 4 to 5 s, and 5 to 6 s are required for the tube to be cleared after the smoke is turned off. These times are comparable to those calculated by dividing the distance between the inlet and the disk by the average linear velocity of the gas.

In other experiments we studied the effects of heating the susceptor disk. For a 10-slpm gas-injection rate through the porous plug, Fig. 7 shows the flow pattern that occurred at 1 atm

Fig. 6—Vertical cross section showing flow pattern at room temperature and pressure of 1 atm obtained for gas injection through a porous plug. Note the uniform flow throughout the reactor.

and a disk temperature of 600°C. The nonlaminar flow is dominated by thermal convection in which gas above the hot susceptor becomes heated and rises upward along the reactor axis. After reaching the top of the reactor, the heated gas cools as it travels downward alongside the air-cooled reactor wall. The cooled gas is then reheated upon reaching the susceptor and the cycle is repeated.

Recirculation in the convection cells increases the gas residence time of the system. We found, however, that a reduction in reactor pressure to below 0.3 atm suppresses the convection cells and returns the flow to a laminar nature similar to that observed when the disk is at room temperature (Fig. 6). This result can be explained in the following manner. Buoyancy-driven convection varies with the Grashof number, which is the ratio of buoyancy to viscous forces in a flow driven by a temperature difference ΔT. The Grashof number Gr is defined by the equation $Gr \equiv g\rho^2 D^3 \beta \Delta T / \eta^2$, in which g = gravitational acceleration, ρ = density, D = tube diameter, β = thermal-expansion coefficient, and η = viscosity. Since β is independent of pressure, ρ is the only quantity in the equation that varies with P. Thus $Gr \propto \rho^2$. Therefore, we expect thermal convection to decrease with decreasing pressure, as was observed. Reducing the reactor pressure P without changing the mass flow rate also increases the gas velocity by a factor of $1/P$. Thus a reduction in P from 1 atm to 0.1 atm would decrease the duration of the initial and final transient response by a factor of 10.

Numerical Modeling

Gas-flow visualization is instrumental in understanding phenomenological effects. Such observation, however, provides a limited basis for predictions of the thickness and compositional uniformity of an epilayer, or the compositional grading of heterostructures. In order to make such predictions, MIT's Department of Chemical Engineering developed a detailed quantitative model to describe the heat and mass transfer and fluid-flow phenomena for a nonisothermal gas mixture in a vertical rotating-disk reactor. Reference 8 contains details of the model formulation

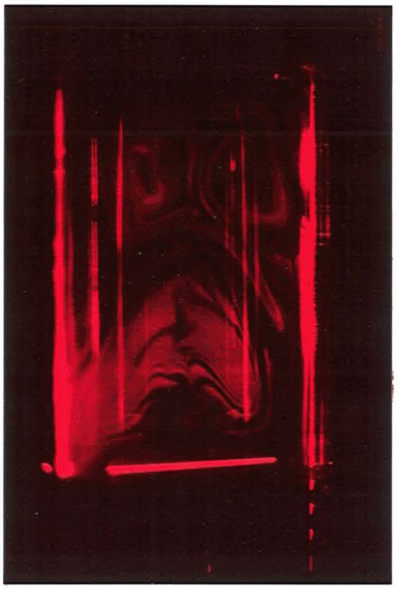

Fig. 7—Vertical cross section showing flow pattern for the case in which the susceptor disk is heated to 600°C. The gas-injection rate through the porous plug is 10 slpm and the pressure is 1 atm. Note that heating the susceptor disk leads to thermal convection.

and solution method.

For simplicity, the analysis decouples the calculation of the flow and temperature fields in the reactor from the calculation of the transport of the reactant species. This simplification requires that the change in gas velocity that results from epilayer growth and the change in the layer shape with time must be small relative to the mean gas velocity. Using standard Galerkin finite-element methods [9, 10], the analysis calculates velocity and temperature fields from conservation of momentum, mass, and energy equations. The fields are then introduced into the time-dependent convection-diffusion equation for the transport of a dilute species with layer growth limited by mass transfer.

To represent the interaction between the temperature and composition fields, the model incorporates the overall gas-phase kinetics for the pyrolysis of the Group III reactant. The kinetic theory for an ideal gas is used to estimate the pressure- and temperature-dependent transport coefficients and thermophysical properties of the gas. The estimation is valid because the concentrations of the dilute species are only 10^{-3}-to-10^{-2} mole percent. The model also includes the effects of thermal diffusion as a mode of species transport. A detailed heat-transfer model that includes conduction and radiation to the quartz reactor wall was necessary for modeling the boundary conditions of the reactor. The dimensions of the modeled system are the same as those of the apparatus used for the flow visualization; no adjustable parameters are used.

Using the numerical methods discussed, we calculated the flow fields for H_2 entering the

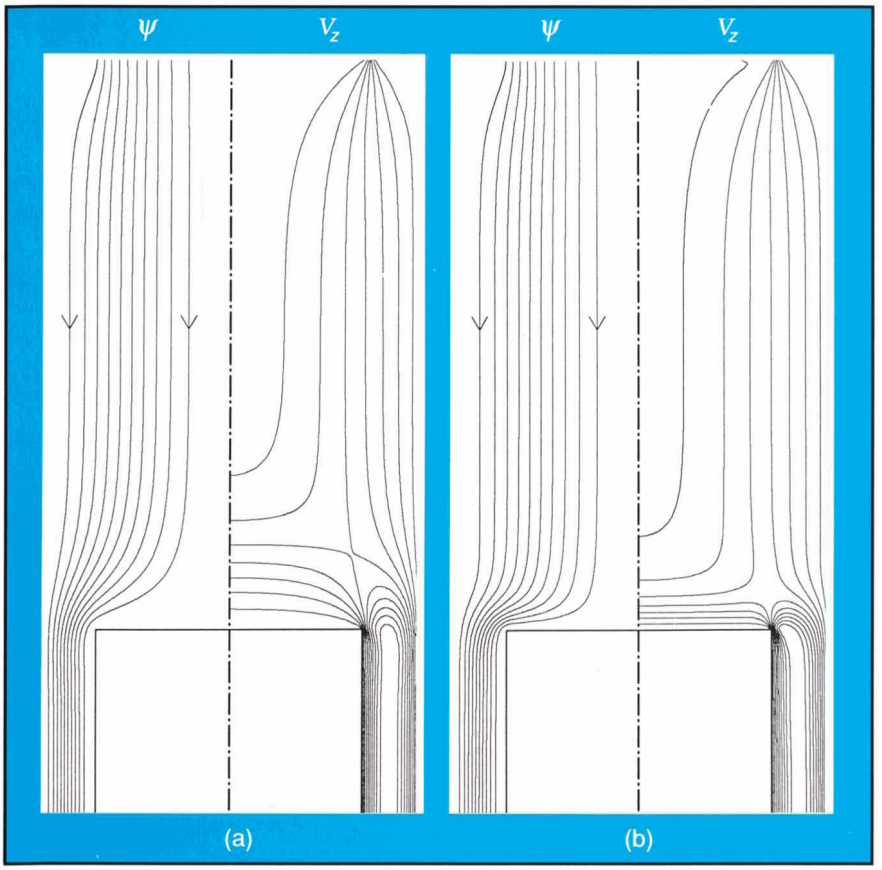

Fig. 8—Flow fields computed for H_2 at P = 1 atm; T = 300 K; and (a) ω = 0 rpm, and (b) ω = 100 rpm. Streamlines (ψ) are shown on the left of each figure and contours of axial velocity (V_z) on the right. Note that rotating the susceptor increases the region over which the boundary layer, which is a function of V_z, is uniform.

OMVPE reactor at 10 slpm, room temperature, and 1 atm (Fig. 8[a]). The left half of Fig. 8(a) shows how the streamlines (ψ) develop from a flat profile at the inlet to a parabolic profile near the susceptor surface. The flow is laminar and sweeps out the entire reactor, as was observed in the flow visualization. As the gas approaches the susceptor, an opposing pressure gradient caused by the susceptor slows down the gas near the reactor axis while the gas near the reactor wall accelerates. This effect results in a stagnation flow in which the profile of V_z (the axial component of the flow velocity, shown in the right half of Fig. 8[a]) is flattened above the susceptor surface. The gas moves radially outward over the susceptor before exiting through the annular gap between the susceptor and the reactor wall. The stagnation flow has a momentum boundary layer adjacent to the susceptor top whose thickness varies in proportion to $V_z^{-1/2}$ [11].

The boundary layer will be uniform in thickness if the velocity field of the impinging gas is uniform. However, the finite radius of the susceptor and the presence of the reactor wall introduce edge effects that result in radial variations in velocity. Contours of the axial component of the velocity V_z, shown in the right half of Fig. 8(a), indicate that the boundary-layer thickness is constant only in a small region near the centerline of the susceptor and decreases toward the edge of the susceptor.

Rotating the susceptor increases the region over which the boundary layer is uniform. Susceptor rotation induces a centrifugal pumping action that pulls the gas down along the centerline and pushes it radially outwards above the susceptor top. Figure 8(b) shows the effect of susceptor rotation for a rotation rate ω = 100 rpm, an H_2 mass flow rate of 10 slpm, and a pressure equal to 1 atm. The pumping action is evident near the top of the susceptor. Note that in comparison with Fig. 8(a), the streamlines are bunched closer to the susceptor top and the thickness of the boundary layer is constant across most of the susceptor surface. As ω is increased, the thickness of the boundary layer decreases and the thickness varies with respect to $\omega^{-1/2}$ [11].

Heating the susceptor leads to convection within the reactor, as was discussed earlier. Figure 9, which shows the effect of susceptor heating for an H_2 mass flow rate of 10 slpm and pressure of 1 atm, plots the flow (ψ) and temperature (T) fields for various susceptor temperatures. Note that a buoyancy-driven, counterclockwise convection cell appears above the susceptor at T = 312 K (Fig. 9[b]). The cell grows when the susceptor temperature is increased to T = 973 K (Fig. 9[c]). At higher temperatures, the cell dominates the flow by pushing the inlet-flow streamlines to the reactor wall.

Susceptor temperature also affects the temperature field within the reactor. Note that upward gas motion along the centerline convects the temperature field upward (Figs. 9[b] and 9[c]), causing a thermal inversion that pushes hot gas near the inlet.

According to the Grashof number, gas pressure in the reactor affects the magnitude of the driving force for convection. We can reduce the intensity of buoyancy-driven convection by decreasing the density differences that are caused by temperature variations. Figure 10 shows the dramatic effect of reduced pressure on buoyancy-driven convection. At a reduced pressure of 0.2 atm (Fig. 10[c]), the buoyancy driving force is small in comparison with the inlet forced flow, which dominates the velocity field. The plots include the effects of susceptor rotation at low speed (ω = 20 rpm), which is often used experimentally to eliminate asymmetries that arise from nonuniform heating by the RF field.

For the conditions of Fig. 10, additional flow fields calculated at various values of ω indicate that the boundary-layer thickness is constant within 2% for ω = 500 rpm, and that rotation is a stabilizing force on the flow. In addition, we found that at ω = 500 rpm, the reactor pressure can be increased to 0.4 atm without the onset of buoyancy-driven convection.

We simulated the growth of a GaAs/AlAs heterostructure under operating conditions chosen to optimize film uniformity (ω = 500 rpm and P = 0.2 atm) and interface abruptness. Figure 11(a) shows the time response of the

epilayer growth rate after the injection of TMG followed 9 s later by the injection of TMA. The growth rate quickly reaches a steady-state value, indicating that the axial dispersion in the reactor (i.e., the intermixing of the TMG with the pure H_2 gas front) at low pressure is minimal. To quantify the interface abruptness predicted by the analysis, we define the interface width as the thickness of epilayer grown while the concentration of the reactant gas changes from 10% to 90% of the steady-state value (Fig. 11[b]). The time Δt over which this change occurs is estimated to be about 0.7 s. By integrating the growth rate over this time interval, we calculate the interface width to be approximately 4 Å, which is on the order of one to two monolayers.

Reactor Design and Evaluation

Design

Figure 12 is a schematic of the OMVPE reactor that was designed and built at Lincoln Laboratory. The reactor consists of a vertical quartz tube and an RF-heated susceptor that can rotate up to 1000 rpm. As with the gas-flow

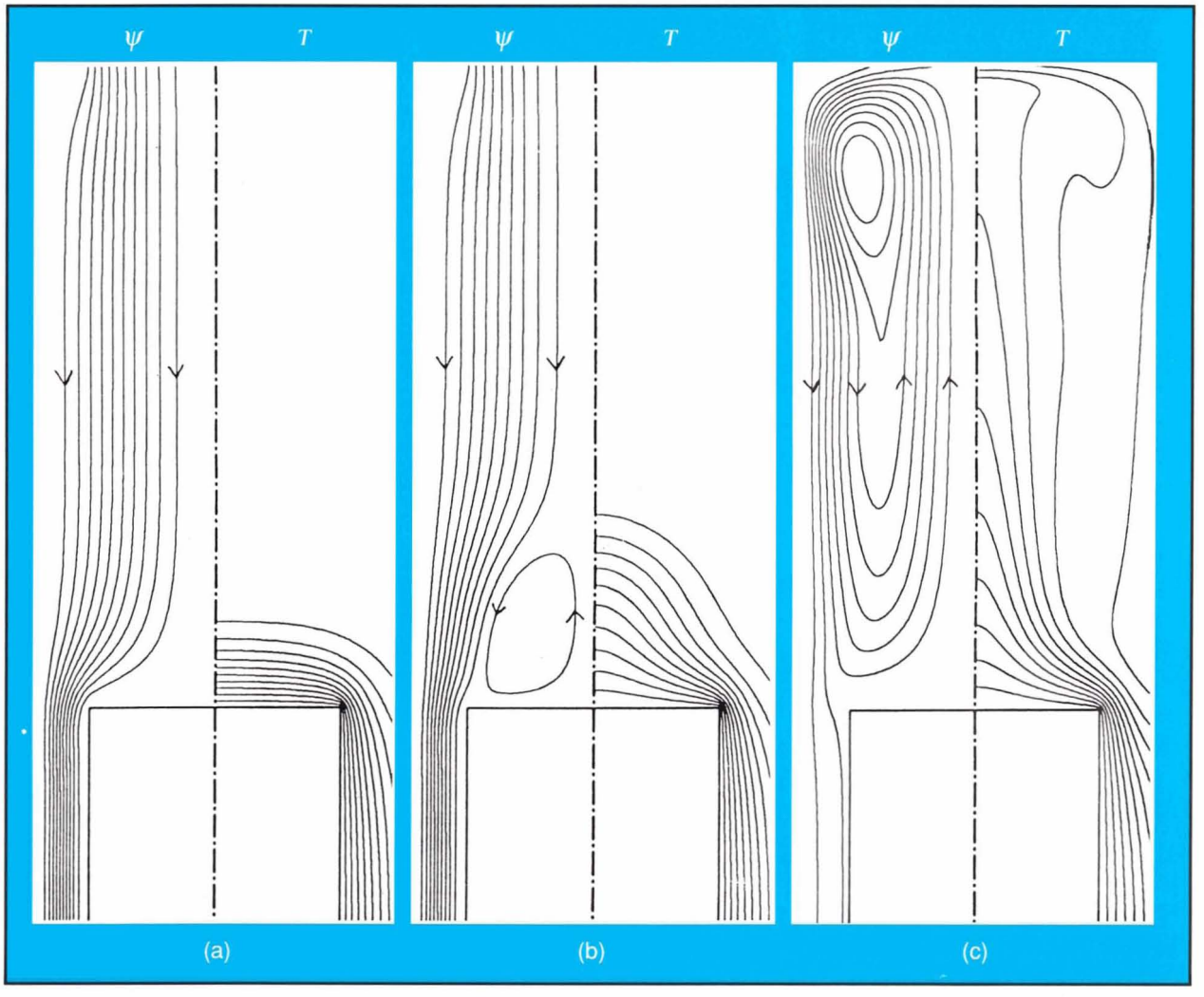

Fig. 9—Effect of susceptor temperature on streamlines (ψ) and temperature (T) contours. The flow fields are computed for H_2 at P = 1 atm; ω = 0 rpm; and (a) T = 300.3 K, (b) T = 312 K, and (c) T = 973 K. Note that heating the susceptor disk leads to thermal convection inside the reactor. The convection causes a thermal inversion that pushes hot gas near the inlet.

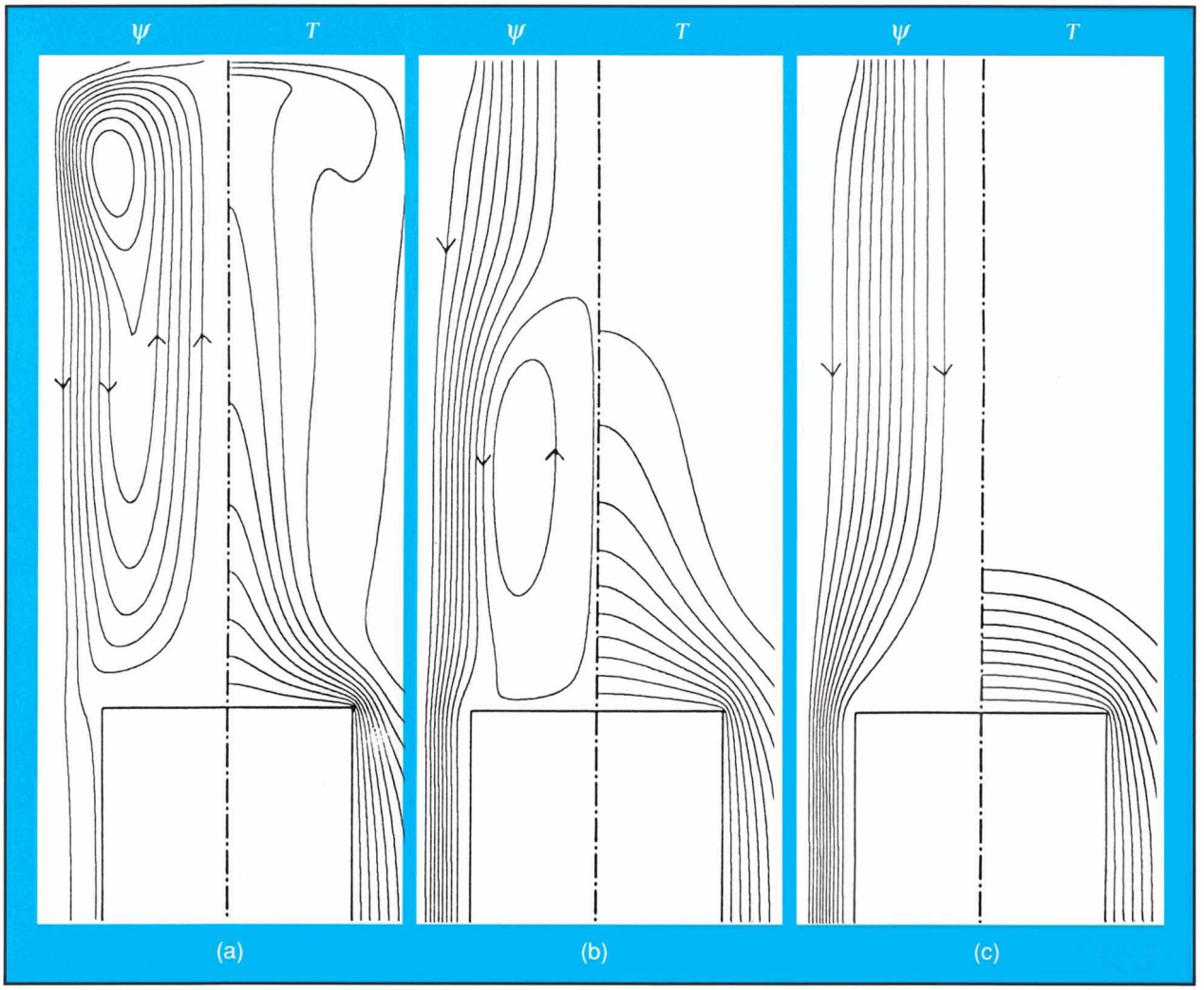

Fig. 10—Effect of reactor pressure on streamlines (ψ) and temperature contours (T) in flow fields computed for H_2 at T = 973 K; ω = 20 rpm; and (a) P = 1 atm, (b) P = 0.26 atm, and (c) P = 0.2 atm. Note that reducing the reactor pressure suppresses the thermal convection inside the reactor.

visualization apparatus, the carrier and source gases are injected through an inlet into an antechamber at the top of the reactor. The inlet is radial with respect to the tube axis, and the antechamber is designed to produce turbulent flow for complete mixing of the component gases. From the antechamber, the gas flows through a stainless steel mesh that ensures plug flow into the reactor tube. Smooth flow past the susceptor is maintained by a purge enclosure that has the same diameter as the susceptor and is situated around the susceptor's rotating shaft. The purge enclosure also protects the rotating seal from GaAs/AlGaAs deposits. After passing the susceptor, gas exits the reactor through exhaust ports located 180° apart.

Substrates are loaded into the system through a glove box situated at the top of the reactor. N_2 is used to purge the glove box of oxygen and water because epilayers grown from precursors that contain aluminum are highly sensitive to those substances.

The center of the susceptor cap is recessed to prevent substrates from flying off the susceptor at high rotation rates. A thermocouple measures the susceptor temperature and an infrared pyrometer allows the continuous monitoring of substrate temperature during epitaxial growth. After a susceptor made of graphite was replaced with one made of molybdenum, the

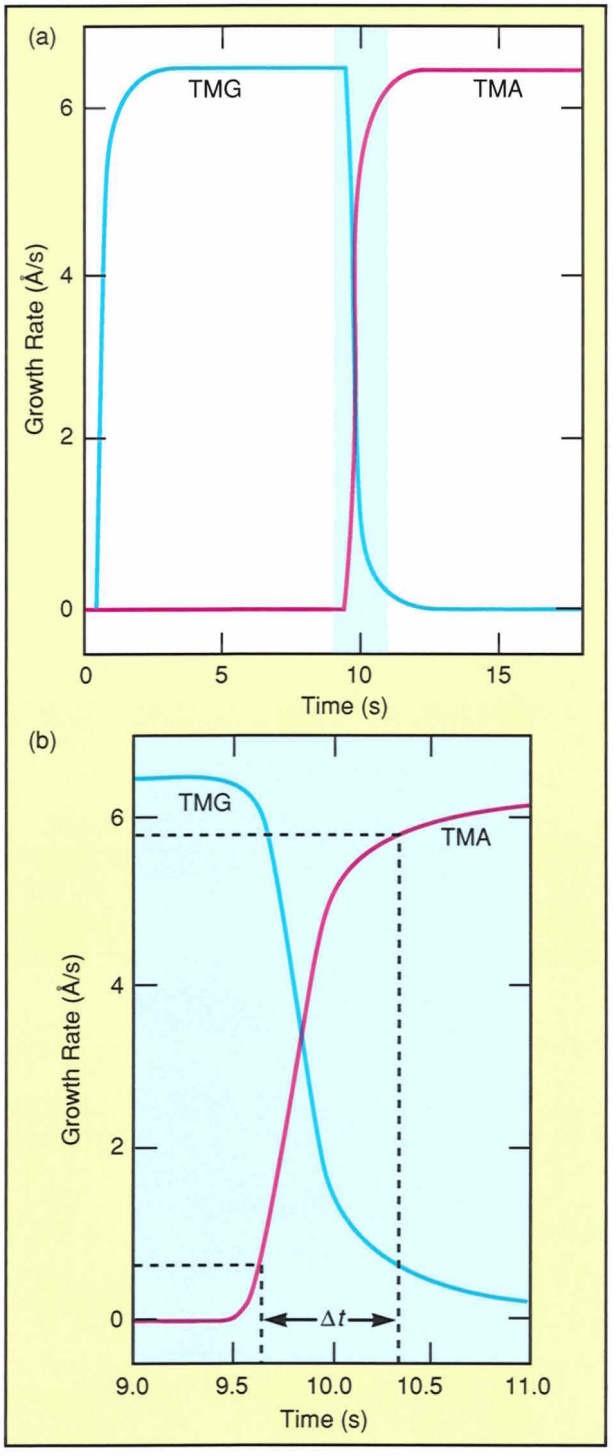

Fig. 11—Simulated time response of the epilayer growth rate after the injection of trimethylgallium (TMG) followed 9 s later by the injection of trimethylaluminum (TMA): (a) Overall time response, and (b) time response for 9.0 s ≤ t ≤ 11.0 s. The interface width is defined as the thickness of epilayer that is grown during Δt, the time in which the concentration of the reactant gas changes from 10% to 90% of the steady-state value.

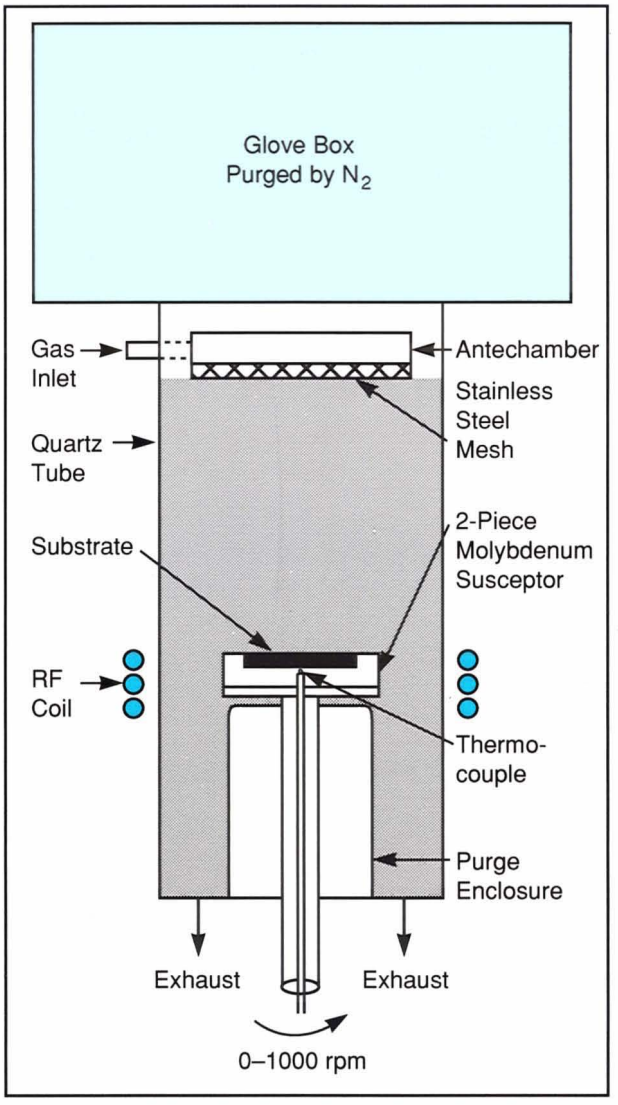

Fig. 12—Schematic diagram of vertical rotating-disk reactor.

temperature uniformity across a 5-cm-diameter GaAs substrate improved from ±6°C to ±2°C.

Test Layers

Using TMG, TMA, and arsine as the source gases, we grew test layers of GaAs and $Al_xGa_{1-x}As$ on GaAs substrates [12]. For ω equal to 20, 200, and 500 rpm, Fig. 13 shows the measured and calculated thickness profiles for 10-μm-thick GaAs layers grown on 5-cm-diameter substrates. The thickness values are normalized with respect to the layer thickness at the center of the substrate. The measured thick-

Table 1. Composition Uniformity of $Al_x Ga_{1-x}$ As Epilayers

PL Peak (nm)	$\bar{x}$	σ	$V = \frac{\sigma}{\bar{x}}$
745.4–745.7	0.1212	2.2×10^{-4}	1.8×10^{-3}
690.3–690.7	0.2280	3.4×10^{-4}	1.5×10^{-3}
660.6–661.0	0.2927	3.3×10^{-4}	1.1×10^{-3}
621.5–622.1	0.3870	6.0×10^{-4}	1.6×10^{-3}

ness near the substrate periphery is greater than at the substrate center by 15% for $\omega = 20$ rpm, 5% for $\omega = 200$ rpm, and 1% for $\omega = 500$ rpm. Since epilayer thickness is inversely proportional to boundary-layer thickness, these results indicate the following: (1) in the absence of susceptor rotation, the velocity of the impinging gas is not uniform across the substrate, and (2) rotation is effective in establishing a uniform boundary layer and uniform velocity profile in which the axial component is constant across the profile. Note that the calculated thickness profiles of Fig. 13 are in very good agreement with experimental data [13].

We can control the composition of the $Al_xGa_{1-x}As$ epilayers by adjusting the ratio of TMA partial pressure to the combined partial pressure of TMG and TMA. The alloy composition will be uniform if the source gases are uniformly dispersed in the reactor and if the fluxes of TMG and TMA through the boundary layer at the substrate are uniform.

To determine the lateral composition uniformity of an $Al_{0.3}Ga_{0.7}As$ epilayer, we measured the photoluminescence (PL) spectra of the epilayer at 31 different locations on half of a 5-cm-diameter wafer. PL is a technique in which carriers in a material are excited by optical photons of higher energy than the material's band gap. As the carriers recombine to a lower energy state, the PL characteristic of the material's band gap can be detected. The x value of the material is then calculated from the peak photon energy. For $\bar{x} = 0.2927$, the standard deviation $\sigma = 3.3 \times 10^{-4}$. The coefficient of variation V, defined as the ratio of σ to $\bar{x}$, is 1.1×10^{-3}. Table 1 summarizes the composition uniformity for $Al_xGa_{1-x}As$ epilayers in which $0.1 < x < 0.4$. In all cases, V is less than or equal to 1.8×10^{-3}.

The composition and partial pressure of the dopant source control the conductivity type and doping level of the GaAs and $Al_xGa_{1-x}As$ epilayers. The p-type dopants are supplied either as liquid OM sources (such as diethylzinc or dimethylcadmium), or gaseous OM sources (such as dimethylzinc) that are diluted in high-purity H_2. The n-type dopants are more often hydrides (such as silane, hydrogen selenide, or hydrogen

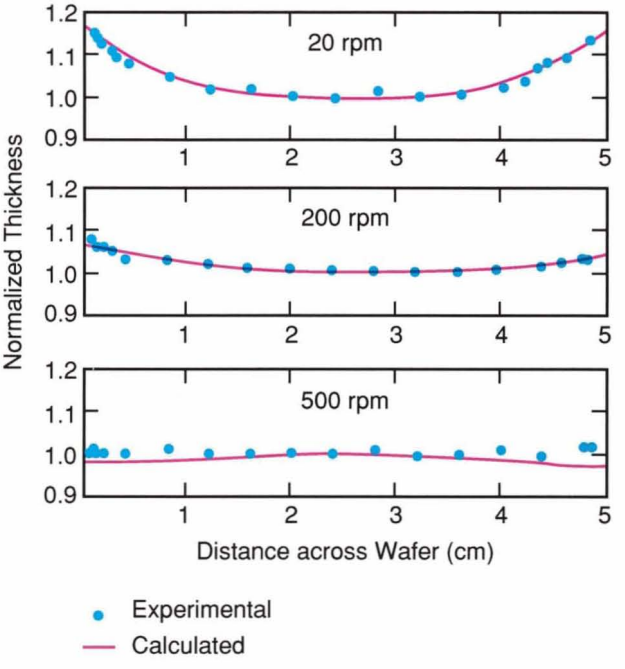

Fig. 13—Experimental and calculated thickness profiles across a 5-cm-diameter substrate for 10-μm-thick GaAs layers grown at rotation rates of 20, 200, and 500 rpm. (The center of the substrate is designated by the x-axis value of 2.5 cm.) The thickness values are normalized with respect to the layer thickness at the center of the substrate. Note that rotation increases the thickness uniformity across the substrate surface.

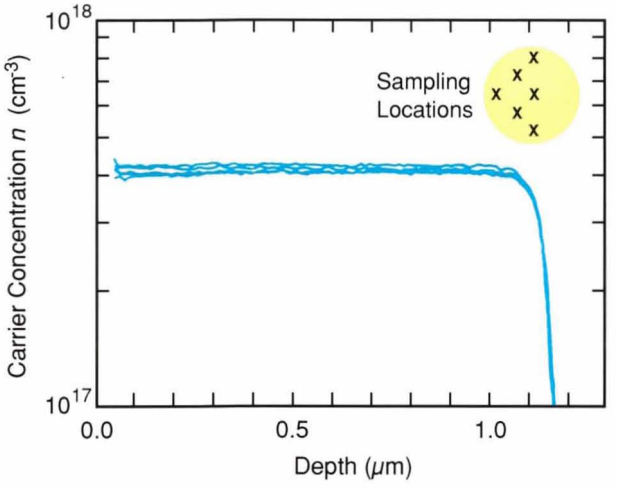

Fig. 14—Carrier-concentration depth profiles for an Se-doped GaAs epilayer. The profiles were measured at six locations on a 5-cm-diameter wafer. The close agreement of the six curves reflects the wafer's high degree of doping uniformity.

sulfide) that are diluted in H_2. The dopants enter the reactor in the same manner as the source gases.

We determined the doping uniformity of GaAs epilayers doped with Se by taking concentration depth profiles [12] of 20 samples from a 5-cm-diameter substrate. Figure 14 shows the profiles of six representative samples. Note that the doping level is constant and uniform throughout the layer. The average dopant concentration is 4.1×10^{17} cm^{-3} and σ is 1.0×10^{16} cm^{-3}. Thus V is 2.4×10^{-2}.

The above thickness, composition, and doping uniformity results are the best reported for OMVPE-grown GaAs and $Al_xGa_{1-x}As$ [14]. Additionally, we have found that ω does not affect the doping and alloy uniformities. This observation suggests the following: the reactant gases are thoroughly mixed in the antechamber before flowing through the stainless steel mesh, and the relative rates of diffusion of the different reactant species in the boundary layer remain constant.

The growth of high-quality GaAs/$Al_xGa_{1-x}As$ heterostructures that have abrupt compositional changes between layers is critical for the fabrication of devices based on quantized electronic states such as the quantum-well diode laser. Figure 15 is a transmission electron

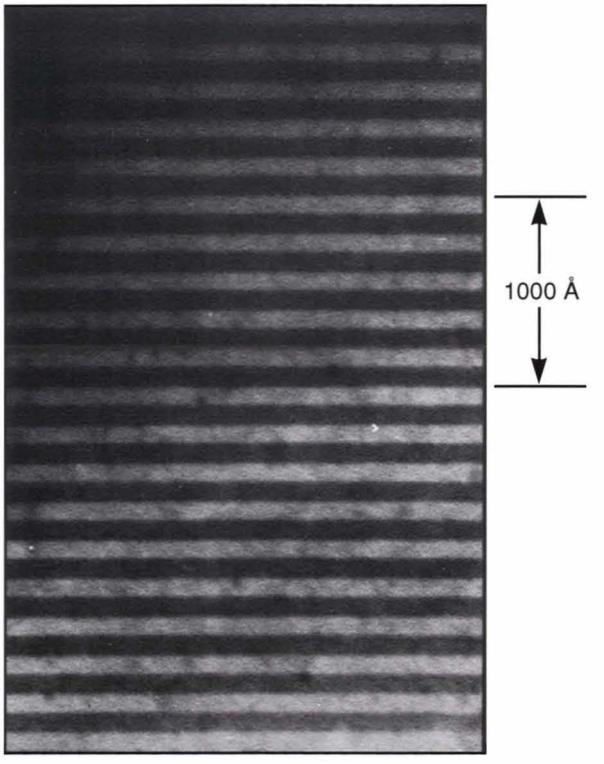

Fig. 15—Transmission electron micrograph of a multiple-quantum-well structure that was grown in the OMVPE reactor. The structure consists of 30 periods of alternating 10-nm layers of GaAs and $Al_{0.3}Ga_{0.7}As$. The $Al_{0.3}Ga_{0.7}As$ layers are the lighter layers.

microscope photograph of a cross section through a multiple quantum-well structure that consists of 30 periods of alternating 10-nm layers of GaAs and $Al_{0.3}Ga_{0.7}As$. The $Al_{0.3}Ga_{0.7}As$ layers are the lighter layers. Even

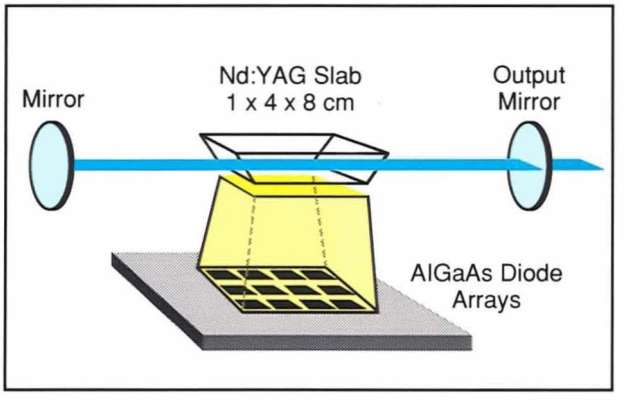

Fig. 16—Schematic diagram of Nd:YAG system. The Nd:YAG solid state laser is being pumped by the AlGaAs diode-laser arrays.

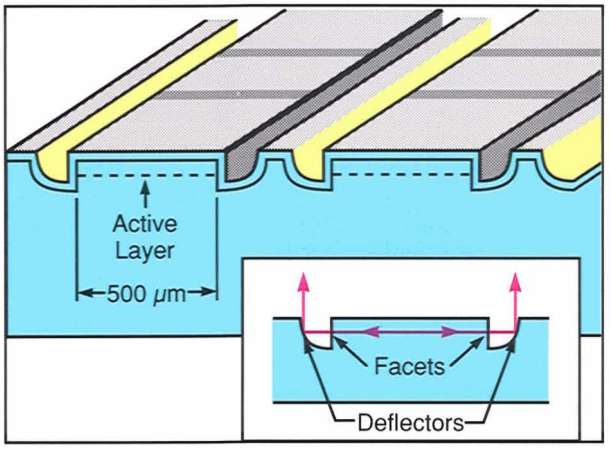

Fig. 17—Schematic diagram of a two-dimensional monolithic surface-emitting diode-laser array. Laser light is deflected 90° by surface-emission deflectors.

on this microscale, the layers exhibit uniform thicknesses throughout the structure and the transitions between layers are sharp. Using PL, we have evaluated the optical quality of such layers and determined their thickness. We have grown high-quality quantum wells as narrow as 2.2 nm, and we have achieved a thickness uniformity falling within one monolayer of GaAs (i.e., 0.28 nm).

Diode Lasers

Arrays of semiconductor diode lasers have applications in laser radar, space communications, optical recording, and optical signal processing and computing. Lincoln Laboratory is developing diode laser arrays for the optical pumping (Fig. 16) of solid state lasers made from Nd:YAG—a neodymium-doped garnet comprised of yttrium, aluminum, and oxide ($Y_3Al_5O_{12}$) [15, 16]. Output radiation from the diode lasers is absorbed by a Nd:YAG slab and reemitted in a series of short, high-power pulses for laser radar applications. In one type of diode laser array—the monolithic two-dimensional surface-emitting array (Fig. 17)—parabolic deflectors etched into the surface of the semiconductor wafer direct the light from the individual lasers in a direction perpendicular to the wafer surface [17, 18].

Figure 18 shows the graded-index separate-confinement heterostructure single-quantum-well (GRIN-SCH SQW) structure that is used for the diode laser arrays. GRIN-SCH SQW lasers are well suited for optical pumping because of their low driving current (i.e., their low thresh-

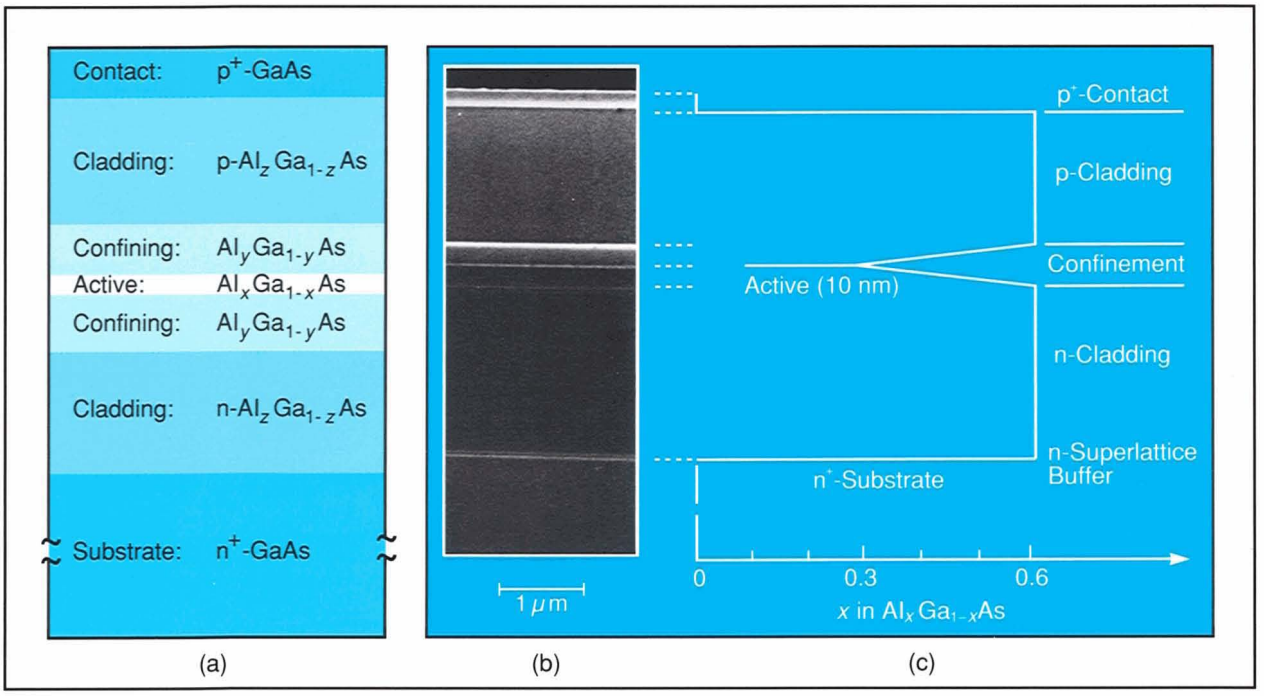

Fig. 18—Structure of the graded-index separate-confinement heterostructure single-quantum-well (GRIN-SCH SQW) laser: (a) schematic diagram, (b) scanning electron microscope cross section, and (c) schematic Al profile.

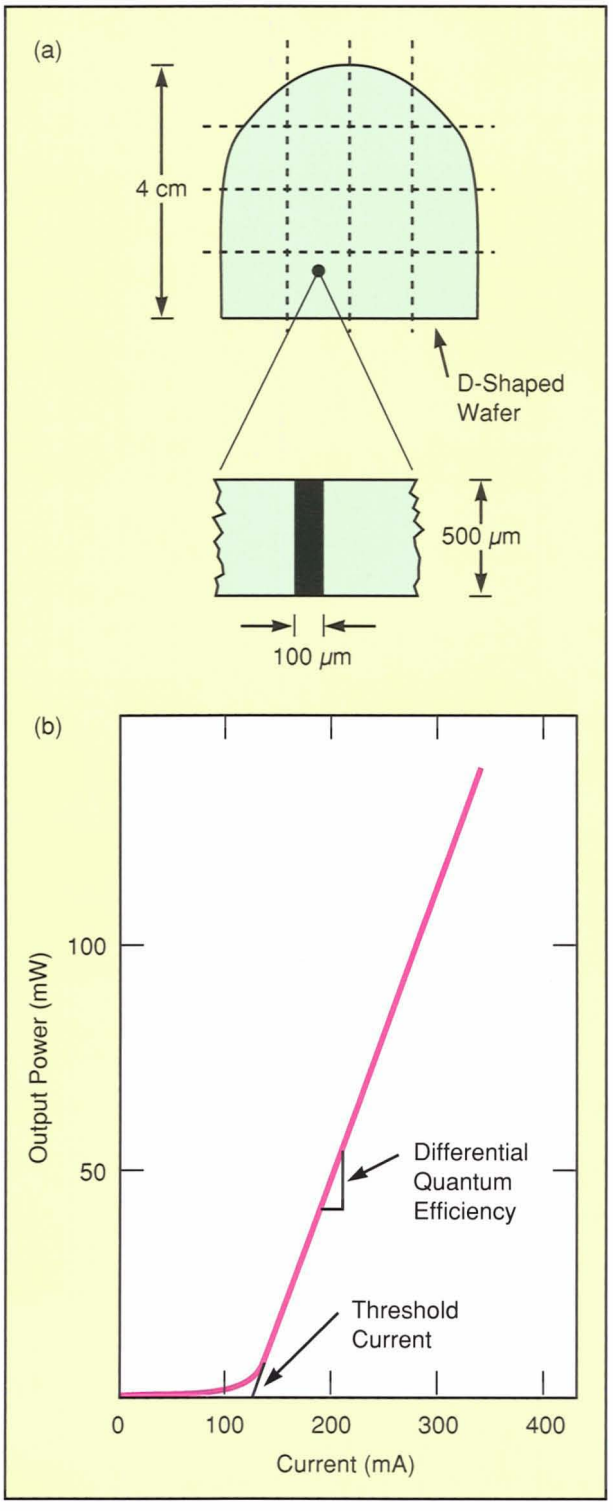

Fig. 19—Evaluation of diode-laser uniformity: (a) sectioning of D-shaped wafer and definition of diode laser device, and (b) typical power versus pulsed current for a broad-area diode laser.

old current density) and high differential quantum efficiency [19].

A schematic diagram (Fig. 18[a]) and a scanning electron microscope photograph (Fig. 18[b]) of a cross section of the GRIN-SCH structure show a series of layers of different compositions and thicknesses. Laser light is generated in the $Al_xGa_{1-x}As$ active layer by the recombination of electron-hole pairs after charge injection across a forward-biased p-n junction. To confine the carriers and the laser light, the value of y in the $Al_yGa_{1-y}As$ confining layers is higher than the x value of the active layer. Because of their higher Al content, the confining layers have (1) a higher band gap, which restricts the carriers to the active layer, and (2) a lower index of refraction, which establishes a waveguide to confine the optical field. The y value in the confining layers increases from a low value at the active-layer boundary to a higher value away from the boundary (Fig. 18[c]), an increase that results in a graded index of refraction. Optical confinement is further enhanced by the $Al_zGa_{1-z}As$ cladding layers, with z equal to the highest value of y.

The efficient pumping of Nd:YAG requires that the spectral output of the diode lasers must coincide with the Nd:YAG absorption band that ranges from 803.5 to 808.5 nm. For the GRIN-SCH structure shown in Fig. 18, an emission wavelength in the required range can be obtained with a 10-nm-thick active layer in which $x = 0.07$.

The emission wavelength is very sensitive to the thickness and composition of the active layer. Therefore, a high degree of uniformity and wafer-to-wafer reproducibility is required in order to obtain satisfactory manufacturing yields. To test laser uniformity, we grew a GRIN-SCH SQW laser structure on a 4-cm × 4-cm D-shaped substrate (Fig. 19[a]) and divided the substrate into 14 sections, each with a nominal area of 1 cm^2. Lasers 100 μm wide were defined by etching away the p^+ contact layer between the devices to reduce current spreading. The laser bars were then cleaved to a cavity length of 500 μm.

We evaluated the performance of the diode lasers by measuring curves of output power versus pulsed current (Fig. 19[b]). From these curves, values of the threshold current density

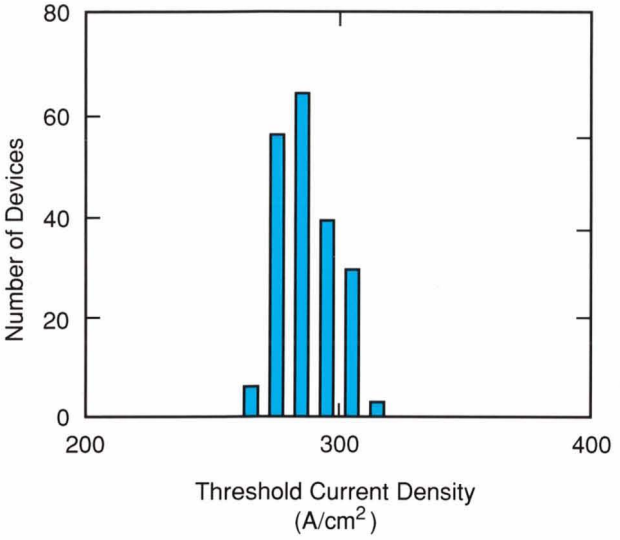

Fig. 20—Distribution of threshold current density (J_{th}) for 192 broad-area lasers. The mean value, standard deviation, and standard deviation divided by the mean value for J_{th} are 287.5 A/cm², 11.3 A/cm², and 0.039, respectively.

J_{th} and differential quantum efficiency η_d were determined. A minimum of 12 devices from each of the 14 1-cm² sections were measured, and Figs. 20 and 21 show the distribution of J_{th} and η_d, respectively, for 192 lasers. For J_{th}, the mean value, σ, and V are 287.5 A/cm², 11.3 A/cm², and 0.039, respectively. For η_d, the mean value, σ, and V are 83.0%, 2.5%, and 0.030, respectively. The highest value of η_d measured is 88%, which is among the highest values reported to date.

Figure 22 shows the distribution of wavelengths for 175 devices that were fabricated from the uniformity-test wafer. The smallest range of wavelengths within a 1-cm × 1-cm section is 0.4 nm and the largest range of wavelengths is 1.2 nm. For all 175 devices, the wavelength mean value, σ, and V are 804.9 nm, 0.6 nm, and 7×10^{-4}, respectively, and the total wavelength range across the wafer is 3.0 nm.

From Ref. 20, we can calculate the change in wavelength with respect to thickness if we assume no variation in Al content in either the active or confining layers. The calculated change is approximately 1 nm per monolayer for an active-layer thickness of 10 nm. Thus the data indicate that over the entire wafer, the active layer does not vary in thickness by more than a few monolayers.

In initial experiments to investigate wafer-to-wafer reproducibility, we measured the operating characteristics of a few lasers from each of nine additional wafers that were grown under the same nominal conditions as the uniformity-test wafer (Table 2). For these lasers, which had cavity lengths of 700 μm rather than 500 μm, J_{th} is lower than that which would be expected from the weak dependence of threshold current on length [21]. This result can be explained by reduced current spreading in the diodes, which were etched down to the active layer. The variability in J_{th} and η_d is most likely to result to a large extent from variations in the details of the fabrication process.

The total range of emission wavelengths for all of the devices studied is only 3.9 nm. The reproducibility of the emission wavelength depends in part on the reproducibility of the thickness and aluminum content of the active layer. Taking into account the MFC run-to-run precision (±0.2 standard cubic centimeters per minute), we expect the reproducibility of the aluminum content to be ±0.2%, which would correspond to a wavelength range of 2 nm. The remainder of the observed wavelength range

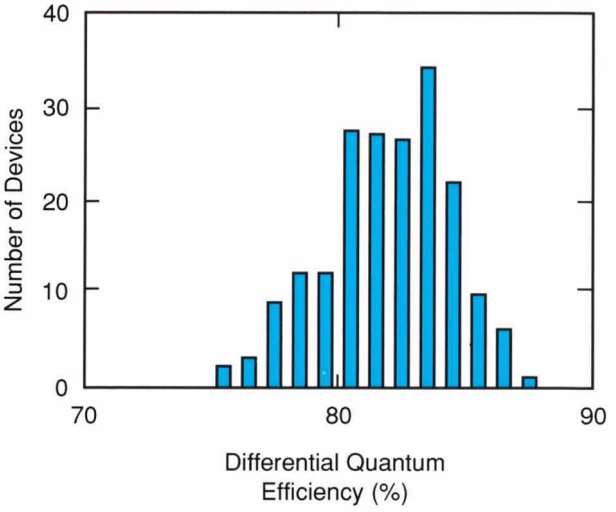

Fig. 21—Distribution of differential quantum efficiency (η_d) for 192 broad-area lasers. The mean value, standard deviation, and standard deviation divided by the mean value for η_d are 83.0%, 2.5%, and 0.03, respectively. The highest value of η_d that we measured is 88%, which is among the highest values reported to date.

Table 2. Properties of Broad-Area Lasers Fabricated from Different Wafers

Run Number	J_{th} (A/cm^2)	η_d (%)	λ (nm)
413	184	62.4	805.5
414	175	79.6	806.5
415	179	85.4	807.2
416*	288	83.0	803.5–806.5
417	179	72.6	805.0
442	192	78.8	804.1
443	184	75.6	804.2
444	184	70.0	807.4
447	178	79.8	804.4
450	169	78.6	806.8

*Uniformity-test wafer (500-μm laser cavity)

Note: The J_{th} values reported are the lowest values per each run. The η_d values are the highest.

(i.e., 1.9 nm) can be accounted for by a thickness variation of a few monolayers.

Summary

We have grown extremely uniform GaAs and AlGaAs epilayers in a vertical rotating-disk OMVPE reactor. The reactor was specially designed by using gas-flow visualization and numerical modeling. A new gas-injection method combined with low-pressure operation produces a laminar flow field and short gas residence times. At low-pressure, high-susceptor rotation rates are necessary for obtaining layers of uniform thickness. To test the reactor, we have fabricated high-performance, broad-area GRIN-SCH SQW diode lasers containing a 10-nm-thick $Al_{0.07}Ga_{0.93}As$ active layer, a structure specifically designed to pump Nd:YAG solid state lasers. The diode lasers have threshold current densities, differential quantum efficiencies, and emission wavelengths that are highly uniform over an area of 16 cm^2. Excellent wafer-to-wafer reproducibility of the emission wavelengths has also been demonstrated.

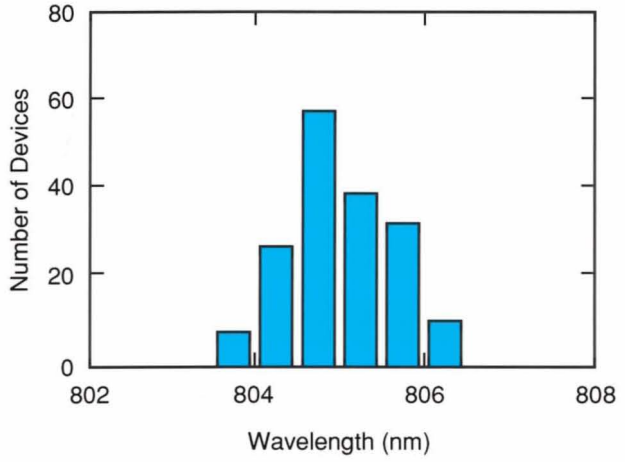

Fig. 22—Distribution of emission wavelength (λ) for 175 broad-area lasers. The mean value, standard deviation, and standard deviation divided by the mean value for λ are 804.9 nm, 0.6 nm, and 7×10^{-4}, respectively.

Acknowledgments

The author gratefully acknowledges the collaborators on this work: S. Patnaik and R.A. Brown for numerical modeling; S.H. Groves, S.C. Palmateer, and D.W. Weyburne for flow visualization; J.W. Caunt for reactor design and fabrication; and H.K. Choi, J.P. Donnelly, and J.N. Walpole for laser development. The author is especially grateful to D.M. Tracy for his assis-

tance in flow visualization and epitaxial growth. The author also acknowledges the contributions of J.H. Mahoney and M.Z. Bistany for flow-visualization photography; G.W. Turner and J.W. Chludzinski for photoluminescence; P.M. Nitishin for scanning electron microscopy and K. Anderson for transmission electron microscopy; and M.K. Connors, D.F. Kolesar, W.L. McGilvary, L.J. Missaggia, and G.D. Silva for diode-laser fabrication and evaluation. The continued interest of A.J. Strauss and I. Melngailis is also greatly appreciated.

References

1. W.D. Goodhue, "Using Molecular-Beam Epitaxy to Fabricate Quantum-Well Devices," *Lincoln Laboratory J.* **2,** 183 (1989).
2. H.M. Manasevit and W.I. Simpson, "The Use of Metal-Organics in the Preparation of Semiconductor Materials," *J. Electrochem. Soc.* **116,** 1725 (1969).
3. G.T. Muhr, D.A. Bohling, T.R. Omstead, S. Brandon, and K.F. Jensen, "Recent Advances in the Development of Arsine Substitutes for Use in Metal Organic Vapour Phase Epitaxy of GaAs," *Chemitronics* **4,** 26 (1989).
4. J.S. Roberts and N.J. Mason, "Factors Influencing Doping Control and Abrupt Metallurgical Transitions during Atmospheric Pressure MOVPE Growth of AlGaAs and GaAs," *J. Cryst. Growth* **68,** 422 (1984).
5. R.S. Sillmon, N. Bottka, J.E. Butler, and D.K. Gaskill, "An Ultra-Fast Gas Delivery System for Producing Abrupt Compositional Switching in OMVPE," *J. Cryst. Growth* **77,** 73 (1986).
6. C.A. Wang, S.H. Groves, S.C. Palmateer, D.W. Weyburne, and R.A. Brown, "Flow Visualization Studies for Optimization of OMVPE Reactor Design," *J. Cryst. Growth* **77,** 136 (1986).
7. T.J. Mueller, "Recent Developments in Smoke Flow Visualization," in *Flow Visualization III*, ed. W.J. Yang (Hemisphere Publishing Corp., New York, 1985), p. 30.
8. S. Patnaik, R.A. Brown, and C.A. Wang, "Hydrodynamic Dispersion in Rotating-Disk OMVPE Reactors: Numerical Simulation and Experimental Measurements," *J. Cryst. Growth* **96,** 153 (1989).
9. Y. Yamaguchi, C.J. Chang, and R.A. Brown, "Multiple Buoyancy-Driven Flows in a Vertical Cylinder Heated from Below," *Philos. Trans. Roy. Soc. London, Ser. A* **312,** 519 (1984).
10. F. Thomasset, *Implementation of Finite Element Methods for Navier-Stokes Equations* (Springer-Verlag, New York, 1981).
11. H. Schlichting, *Boundary Layer Theory* (McGraw-Hill, New York, 1979).
12. C.A. Wang, S. Patnaik, J.W. Caunt, and R.A. Brown, "Growth Characteristics of a Vertical Rotating-Disk OMVPE Reactor," *J. Cryst. Growth* **93,** 228 (1988).
13. S. Patnaik, "Modelling of Transport Processes in Chemical Vapor Deposition Reactors," Ph.D Thesis, Dept. of Chemical Engineering, MIT, Cambridge, 1989.
14. C.A. Wang, H.K. Choi, and M.K. Connors, "Large-Area Uniform OMVPE Growth for GaAs/AlGaAs Quantum-Well Diode Lasers with Controlled Emission Wavelength," *J. Electron. Mater.* **18,** 695 (1989).
15. J.P. Donnelly, K. Rauschenbach, C.A. Wang, W.D. Goodhue, and R.J. Bailey, "Two-Dimensional Surface-Emitting Arrays of GaAs/AlGaAs Diode Laser Arrays," in *Laser Diode Technology and Applications*, ed. L. Figueroa, *Proc. SPIE* **1043,** 92 (1989).
16. T.Y. Fan and R.L. Byer, "Diode Laser-Pumped Solid-State Lasers," *IEEE J. Quantum Electron.* **24,** 895 (1988).
17. Z.-L. Liau and J.N. Walpole, "Mass-Transported GaInAsP/InP Lasers," *Lincoln Laboratory J.* **2,** 77 (1989).
18. J.P. Donnelly, W.D. Goodhue, T.H. Windhorn, R.J. Bailey, and S.A. Lambert, "Monolithic Two-Dimensional Surface-Emitting Arrays of GaAs/AlGaAs Diode Lasers," *Appl. Phys. Lett.* **51,** 1138 (1987).
19. W.T. Tsang, "A Graded-Index Waveguide Separate-Confinement Laser with Very Low Threshold and a Narrow Gaussian Beam," *Appl. Phys. Lett.* **39**, 134 (1981).
20. J.P. Donnelly, private communication.
21. P.S. Zory, A.R. Reisinger, L.J. Mawst, G. Costrini, C.A. Zmudzinski, M.A. Emanuel, M.E. Givens, and J.J. Coleman, "Anomalous Length Dependence of Threshold for Thin Quantum Well AlGaAs Diode Lasers," *Electron. Lett.* **22**, 475 (1986).

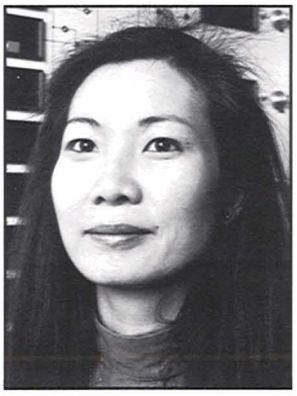

CHRISTINE A. WANG is a staff member in the Electronic Materials Group at Lincoln Laboratory. Her research interests include the development of OMVPE technology, crystal growth of III-V semiconductors by OMVPE, and the development of semiconductor quantum-well laser structures. Christine received the following degrees from MIT: an S.B. in materials science and engineering, an S.M. in metallurgy, and a Ph.D. in electronic materials. She is a member of Tau Beta Pi, Sigma Xi, and the American Association of Crystal Growth.